

NATURAL HAZARDS

Surface deformations of the 6 February 2023 earthquake sequence, eastern Türkiye

Jiannan Meng^{1,2†}, Timothy Kusky^{1,2,3*}, Walter D. Mooney^{4*}, Erdin Bozkurt³, Mehmet Nuri Bodur⁵, Lu Wang¹

Two powerful earthquakes struck Türkiye on 6 February 2023. The initial rupture was on the Dead Sea fault zone, yet maximum displacements and energy release [moment magnitude (M_w) 7.8] occurred 24 seconds later when rupture transferred to the East Anatolian fault zone (EAFZ). More than 7 hours later, a M_w 4.5 aftershock at the junction of the EAFZ with the east-west striking Çardak-Sürgü fault was followed 86 minutes later by the second large (M_w 7.5) earthquake, suggesting a causal relationship. We provide quantitative ground and aerial documentation of surface offsets and kinematics from the slipped faults, providing important data on surface deformation during large continental strike-slip earthquakes, rupture propagation mechanisms, and how slip may be transferred between complex fault systems. We also provide insight into how slip along linked fault systems accommodates global plate motions.

Large earthquakes in populated regions are responsible for some of the greatest disasters in human history. In epicentral regions on land, obtaining valuable early field observations is often prevented by infrastructure destruction, rescue and recovery operations, hazardous strong aftershocks, inaccessibility, and rapidly eroding fault-scarp features. Despite these challenges, a limited number of studies have been able to correlate

point observations of surface ruptures with overall fault displacements (1–4). The pair of destructive earthquakes of 6 February 2023 in Türkiye (Fig. 1) were densely measured by numerous seismic stations locally and globally, providing a wealth of seismic information. We were able to access the epicentral regions beginning 1 day after these earthquakes; we completed detailed surface mapping of fault ruptures, slip lineations, and offsets along the

new fault traces and obtained an uncommonly detailed view of surface deformation features before postseismic deformation and erosion.

The first event (Pazarcık earthquake) occurred at 4:17 a.m. (local time) with a moment magnitude (M_w) of 7.8, making it the strongest earthquake in Türkiye in the past century (5). The results were catastrophic (figs. S1 to S3), with the devastation of entire cities and officially more than 59,000 deaths (6, 7). The M_w 7.8 fault rupture extended about 350 km (8) along the northeast-southwest-oriented East Anatolian fault zone (EAFZ) (Fig. 1). The second (Elbistan) earthquake (M_w 7.5) occurred 9 hours later, at 13:24 (local time), rupturing an estimated 170 km of the approximately east-west-oriented Çardak-Sürgü fault zone (Ç-SF) (6, 9). Previous geologic

¹State Key Laboratory of Geological Processes and Mineral Resources, Center for Global Tectonics, School of Earth Sciences, China University of Geosciences, Wuhan 430074, China. ²Badong National Observatory and Research Station for Geohazards, China University of Geosciences, Wuhan, Wuhan 430074, China. ³Department of Geological Engineering, Middle East Technical University, Ankara 06800, Türkiye. ⁴US Geological Survey, Menlo Park, CA 94025, USA.

⁵Faculty of Civil Engineering, Hakkari University, Hakkari 30000, Türkiye.
*Corresponding author. Email: tkusky@gmail.com (T.K.); mooney@usgs.gov (W.D.M.)

†These authors contributed equally to this work.

Fig. 1. Location of the M_w 7.8 Pazarcık and M_w 7.5 Elbistan 6 February 2023 earthquakes of the East Anatolian fault system. Aftershocks (blue circles) during the first week after the 6 February 2023 earthquakes and historical earthquakes along the East Anatolian fault are shown. NAF, North Anatolia fault zone; EAF, East Anatolian fault zone; DSF, Dead Sea fault zone; K, Karlova; Ç-SF, Çardak-Sürgü fault zone; CT, Cyprus Trench. The East Anatolia and North Anatolia faults converge at the point where three plates (Anatolia, Arabia, and Eurasia) meet near Karlova, known as the Karlova triple junction (K). The East Anatolian fault, the Dead Sea fault, and the Cyprus Trench meet the Kahramanmaraş triple junction near the first, M_w 7.8 earthquake, at an imprecisely defined location, where the Arabian, African, and Anatolian plates meet. [Sources: faults (10); digital topography (58); recent and historical seismicity (5)]

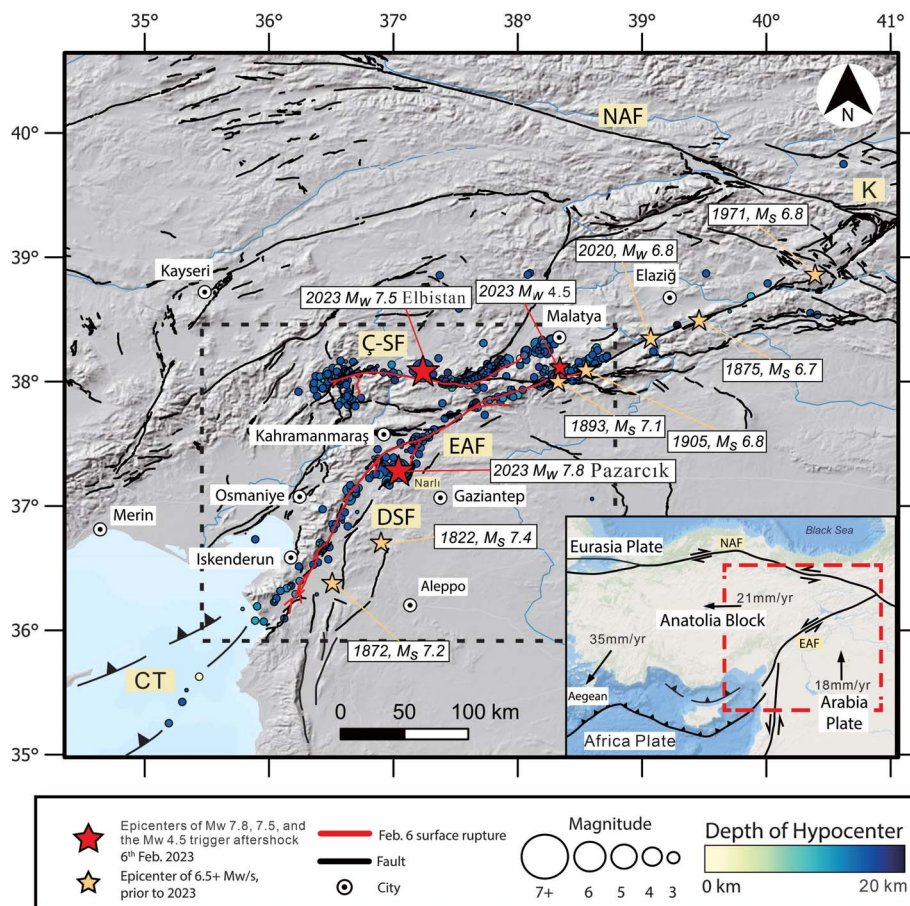
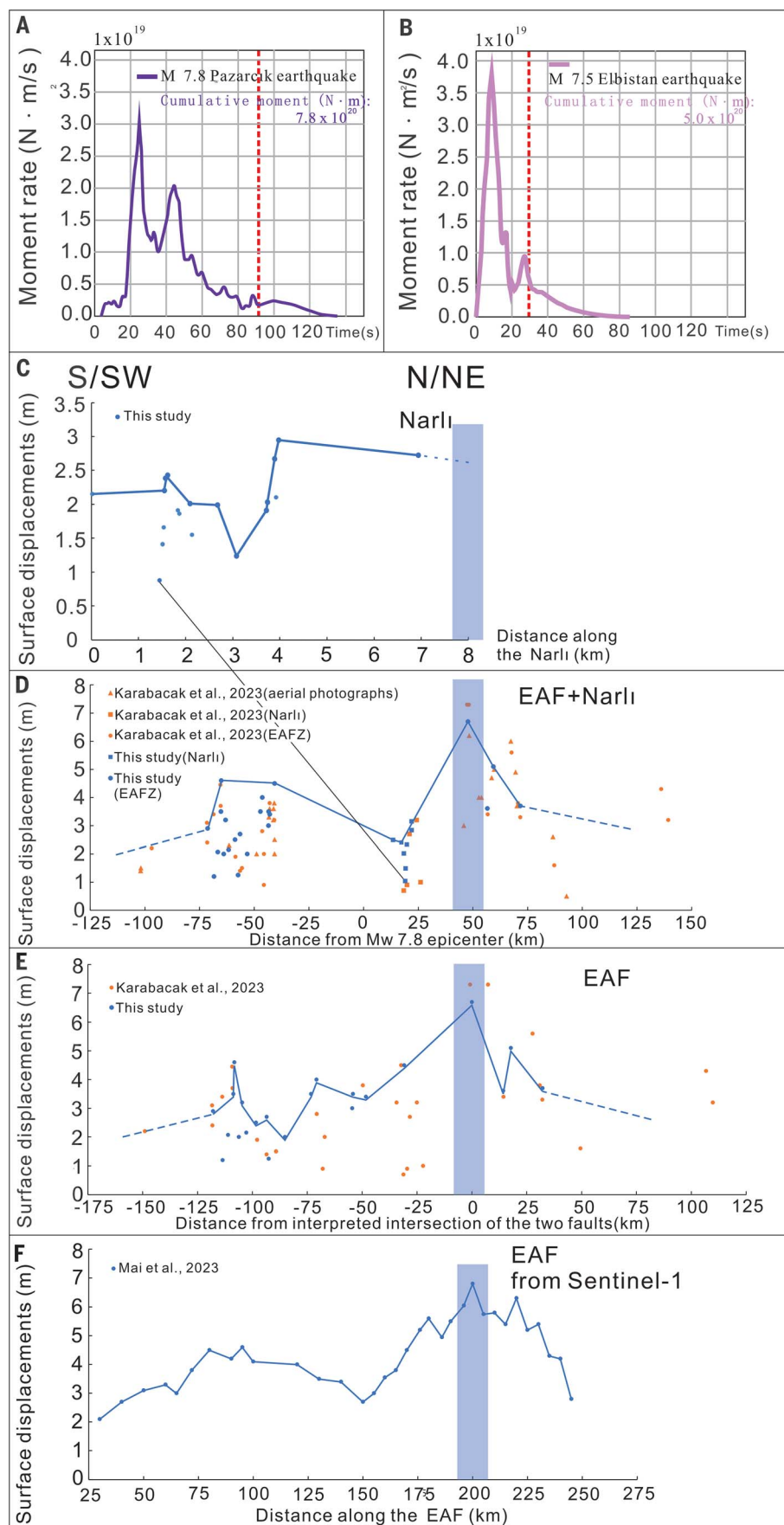


Fig. 2. Energy release spectra compared with displacements measured by field mapping and estimated displacement profiles from field and Sentinel-1 satellite data. (A and B) Seismic moment release versus time for the (A) M_w 7.8 Pazarcık earthquake and (B) M_w 7.5 Elbistan earthquake of 6 February 2023. In the first M_w 7.8 event, the seismic moment remained very low for the first 16 s and then accelerated rapidly, reaching a peak 24 s after initiation. The rupture became bilateral, and a second peak in seismic moment release occurred at 44 s. The red dashed line indicates the time when the rupture ended, with later moment release being scattered energy. The seismic moment of the second M_w 7.5 event reached its peak in less than 10 s. Data are from the US Geological Survey reported in (29). (C to F) Displacements along the ruptured fault segments, with the thin blue line indicating the maximum measured displacement profile estimated from the field observations reported here. The vertical blue column indicates the intersection region of the Narlı segment of the Dead Sea fault (DSF) and the EAFZ. (C) Measured displacements along the Narlı segment, and (D) the Narlı plus EAFZ, plotted against distance from the epicenter (0 km). The thin line connecting (C) and (D) points to the same blue data point. (E) Displacements along the EAFZ (excluding Narlı) plotted versus distance (+ is to northeast, – is to southwest) from fault intersection zone (table S1) (59). (F) Displacements from Sentinel-1 satellite data plotted along the length of the EAFZ (9). The maximum displacements occur near the intersection of the Narlı segment of the DSF and the EAFZ, at a distance of 47.5 km from the epicenter. Assuming that the maximum displacements occurred when and where the maximum energy was released at 24 s after the initial rupture, we estimate that the rupture propagated at 2.03 km/s.



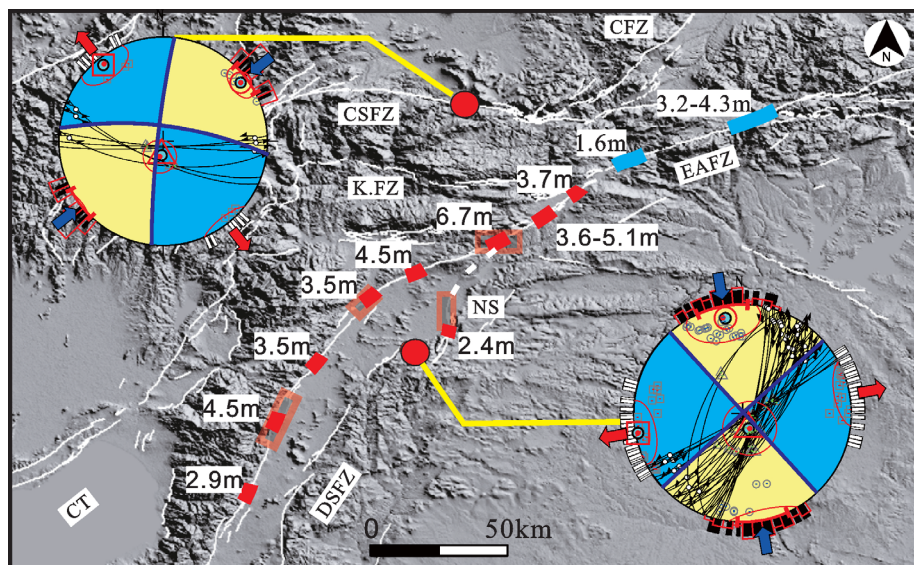


Fig. 3. Field observation of ground offsets and kinematic features around the earthquake area.

Shown is the area identified with the black dashed rectangle in Fig. 1. The map superimposes the regional active fault map (10) over a digital elevation model (24), with measured offsets from our field survey. Offsets labeled with red boxes are from our field observations (table S1), whereas those labeled with blue boxes are compiled from other publications (table S1). The orange rectangles indicate the location of the drone maps [(11), data S1 and S2]. The first, M_w 7.8 event occurred on the Narlı segment (NS) of the Dead Sea fault zone (DSFZ), ~47.5 km southwest of the triple junction region between the DSFZ, EAFZ, and Cyprus Trench (CT), where the African, Anatolian, and Arabian plates meet (7). (Insets) Plots of the earthquake mechanism solutions on lower-hemisphere Schmidt projections (blue, compressional; yellow, extensional) together with our fault kinematic measurements [blue arrows indicate direction of σ_1 , and red arrows indicate σ_3 , calculated by using the methods of (60)]. The blue dots with circles, triangles, and rectangles indicate the directions of σ_1 , σ_2 , and σ_3 , respectively, and the thin red lines indicate the uncertainties (mean cone angle, 1σ SD). The black and white lines on the outside of the plot indicate the maximum and minimum horizontal stress axes, respectively. The thin great circles are the fault planes, and the arrows on it indicate the slip motions, showing a general consistency but a slight discrepancy related to the surface faults being en echelon splays that likely merge with single faults at depth [(32), doc. S2]. NS, Narlı segment of the northern branch of the Dead Sea transform fault; CSFZ, Çardak-Sürgü fault zone; CFZ, Ciglik fault zone; KFZ, Kahramanmaraş fault zone. The white dashed line indicates our interpretation from published active fault maps (10). The maximum measured displacement of 6.7 m occurs at the intersection of the Narlı segment of the DSFZ and the EAFZ, 47.5 km from the epicenter. Comparison with Fig. 2 shows that the maximum displacement occurred when the smaller slip on the Narlı segment of the DSFZ transferred to the EAFZ at the moment of peak energy release 24 s after the initial rupture, activating the entire EAFZ. More fault kinematic data on specific locations are provided in fig. S4.

mapping (10) indicated that the eastern terminus of the Ζ-SF merges into the EAFZ, and the second main earthquake occurred shortly (86 min) after an aftershock (M_w 4.5) of the first event struck the junction of the two faults [(11), imagery S1].

These dual (9) earthquakes and aftershocks, known as the Kahramanmaraş earthquake sequence (6), are associated with various complex strands of the left-lateral Dead Sea fault system, East Anatolian fault system, and their related faults. These faults form the complex and evolving boundaries of the Kahramanmaraş triple junction between the Arabian, African, and Anatolian tectonic plates (6, 7, 12, 13). Along these boundaries, the Arabian plate is sliding northward at 18 mm/year relative to the African plate on the Dead Sea transform fault and colliding with the Eurasian plate, whereas the

African plate is subducting northward beneath Anatolia in the Cyprus Trench, and the Anatolian plate is extruding westward at 21 mm/year along the East Anatolian and North Anatolian transform faults (Fig. 1) (14–24). The earthquake sequence can be described simply in a plate tectonic framework as the Arabian plate taking a step to the north, and the Anatolian plate responding with a jump to the west (7). The data and observations we report here provide a snapshot of the surface deformation patterns related to the lateral movement of tectonic plates. When linked with recordings and interpretations of the same phenomena through geophysical instrumentation, these data and observations provide valuable multiscale and multidisciplinary perspectives. They also may provide insight into interpreting plate tectonic movements recorded in the geological and seismic record,

along with rupture mechanisms along intracontinental plate boundaries and how slip is transferred from one complex plate boundary fault system to another. Further, our observations could ultimately help to protect populations that live in other potentially vulnerable plate boundary regions by informing building codes and preparedness exercises.

Seismological background and earthquake characteristics

The history of strong earthquakes on the central and southern East Anatolian fault is well documented (25, 26). The previous largest event [surface wave magnitude (M_s) 6.8] in the 20th century occurred in 1905 (Fig. 1). More recently, an earthquake of M_w 6.7 occurred on 24 January 2020 on the northeastern portion of the East Anatolian fault system (Fig. 1). Geodetic data indicate that the strain rate on the central portion of the East Anatolian fault is about 10 mm/year (26, 27). Assuming this strain rate, the ~6 m of slip that occurred during the M_w 7.8 earthquake would require 600 years to accumulate. However, strain rates may have varied, and several other earthquakes released some of the strain over this time interval. Paleoseismic data yield an average recurrence interval of 190 years over the past 3800 years (28).

Seismic focal mechanisms indicate that the M_w 7.8 and M_w 7.5 events occurred on nearly vertical strike-slip faults (29). Aftershocks are largely restricted to the upper 20 km (Fig. 1) of the crust, below which crustal displacements are accommodated by ductile deformation. The initial focal depth for the M_w 7.8 earthquake was 10 km (6), and the energy release spectra suggest that it took 10 to 20 s for the rupture to affect the entire upper brittle crust, as the initial rupture propagated north to the EAFZ and south along the Narlı segment of the Dead Sea fault zone (29). The depth extent of aftershocks reveals the rupture width (depth) multiplied by the rupture length (along strike) that defines the total surface area of the rupture. The amount of energy released during the earthquake is proportional to the seismic moment, defined as

$$M_o = \mu D A \quad (1)$$

Where μ is the average shear modulus along the fault, D is the average displacement on the rupture plane, and A is the surface area of the rupture plane.

Estimates of the lengths of the fault rupture for the two 6 February 2023 earthquakes from the distribution of aftershocks and satellite-based optical remote sensing images of displacement (Fig. 1) yield fault rupture lengths of $\sim 350 \pm 30$ km, depth of 20 km and $\sim 170 \pm 20$ km, depth of 20 km for the M_w 7.8 and M_w 7.5 earthquakes, respectively (8, 9, 29, 30). However, the rupture lengths vary depending on which remotely sensed data or geophysical

model is used (37). Using our field data reported here and Eq. 1, we estimated an average slip on the EAFZ of 3.2 m, and on the basis of Sentinel-1 data, the average displacement for the M_w 7.5 rupture of the C-SF is 4.2 m (8, 29). Using Eq. 1 and a shear modulus of 3.5×10^{10} N/m 2 , the seismic moment (M_o) of the M_w 7.8 and M_w 7.5 earthquakes is 7.8×10^{20} and 5.0×10^{20} N·m, respectively.

The rate of seismic moment release during an earthquake helps to determine the duration and amount of energy released. Seismic data reveal the timing of the seismic moment release from the fault rupture plane (29). The timing of seismic moment release indicates that the M_w 7.8 event grew over a period of 24 s (Fig. 2A), when the energy release peaked. We interpret this time to be when the rupture had propagated from the Narli segment of the Dead Sea transform to the East Anatolian transform. From there, the rupture became bilateral along the EAFZ, propagating 125 km to the northeast and 175 km to the southwest (29). The M_w 7.5 event peaked much faster (Fig. 2B), with the rupture propagating bilaterally roughly 55 km both east and west (29) within the first 9 s. The rapid peak in the seismic moment rate suggests that the C-SF was nearly at the rupture stage when it was activated by stress changes from the M_w 7.8 event and associated aftershocks.

Ground and uncrewed aerial vehicle (drone) mapping of fault ruptures

We obtained detailed observations of the surface deformation features, including fault displacement and ground ruptures, and were able to compare our ground-based results with satellite and seismic data as well as with geophysical models for the two large earthquakes. After initial reconnaissance, logistical arrangements, and ground-based observations starting the day after the earthquakes, our quantitative drone-based field mapping started 10 days after the earthquakes [(32), doc. S1]. This allowed us to extract kinematic and displacement data from fault planes in surface soils, rocks, and human constructions such as roads, fences, farm field borders, railroads, and buildings. Many of these features were quickly eroded by rains or destroyed by reconstruction after the earthquakes. We investigated most of the length of the rupture along the EAFZ, extending more than 300 km (Fig. 3). In addition to our surface observations, we also report detailed georeferenced maps of surface ruptures of four key places, imaged with the Real Time Kinematic Drone (DJI Phantom 4 RT). These data complement our ground observations of the deformation features recorded in the days immediately after the earthquakes (figs. S4 to S6 and tables S1 and S2) [(31), drone imagery S2 to S7 and data S1 and S2].

The structural and tectonic setting is complex near the epicentral regions. Three fault

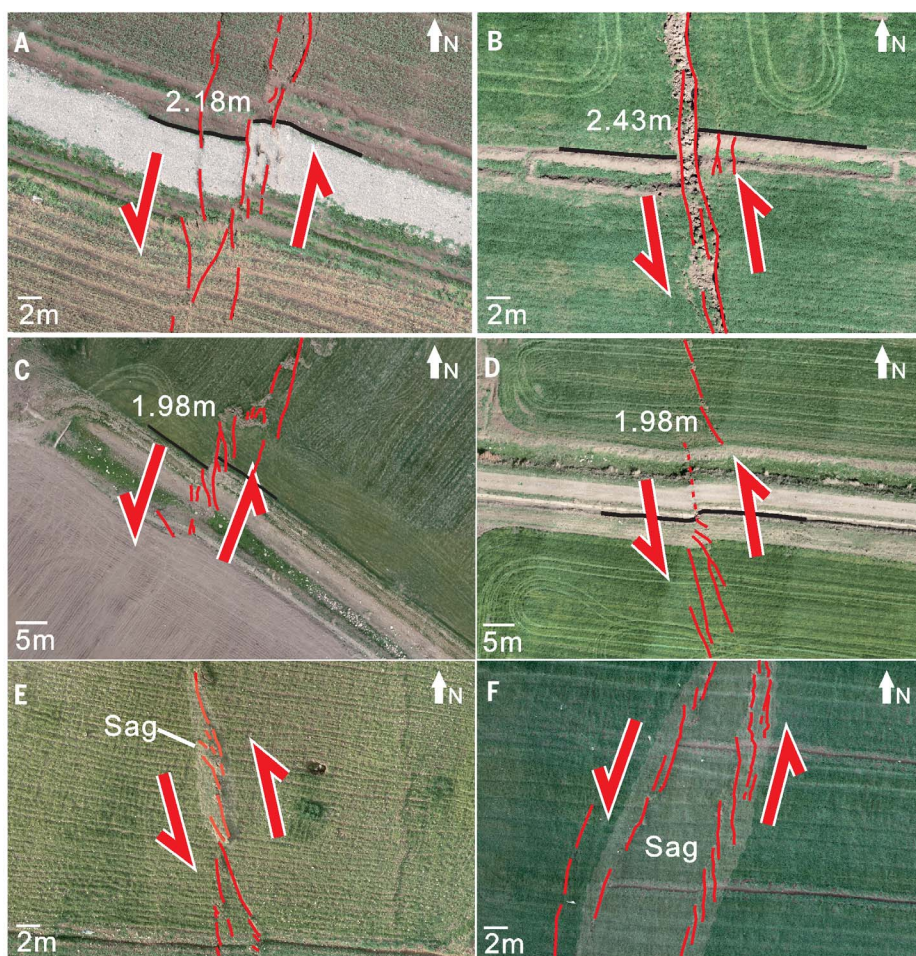


Fig. 4. Horizontal ground offsets and ruptures of the Narli segment of the Dead Sea transform fault.

Images are from aerial drone mapping. Exact locations and other parameters of all images are available in (11), data S1. The locations of the drone mapping areas are shown in Fig. 3. (A) A road with a 2.18-m offset. Black lines are used as a reference. Thin red lines indicate the deformation pattern, and the arrows indicate the motion direction. (B) The field edge with a 2.43-m offset. Black lines are used as a reference. Thin red lines indicate the deformation pattern, and the arrows indicate the motion direction. (C) A road with a 1.98-m offset. Black lines are used as a reference. The field in the southwest part of the image is already plowed over, removing all traces of the fault trace. Thin red lines indicate the deformation pattern, and the arrow indicates the motion direction. Synthetic en echelon faults formed at a low angle to the main ruptures, antithetic faults are at high angles to the main fault, and through-going connecting faults link the different segments. These typically are best developed in a several-meter-wide damage zone, marking the main fault trace. There are some ground distortions and rotations between the ground ruptures. (D) The road with a 1.98-m offset. Black lines are used as a reference. Thin red lines indicate the deformation pattern, and the arrow indicates the motion direction. The north-northeast "lines" are artifacts of the image merging. The location of (D) is close to the edge of the fault segment; the deformation is not as strong as in (A) to (C). (E and F) Distributed en echelon ruptures and also small sag basins related to the strike-slip fault. Scale bars provided at bottom left, (A) to (F).

systems are involved (10), including the main (transform) EAFZ, the Narli fault segment of the Dead Sea transform fault (33, 34), and the east-west C-SF (Fig. 3), which merges into the EAFZ along a fault branch known as the Stürgü fault (10). The M_w 7.8 earthquake initiated on the Narli fault (6). The main C-SF slipped 9 hours after the first event, resulting in the second, M_w 7.5 event of the sequence (6), but the Stürgü fault became inactive, and aftershocks next migrated northeast along a new rupture (Ciglik

fault) parallel with the main EAFZ (Figs. 1 and 3) [(11), imagery S1].

Measured ground offsets

Ground offsets (horizontal) along all three faults are sinistral, varying from <2 to 6.7 m in different locations (Fig. 3 and fig. S4) [(11), data S1 and S2]. According to our field observations, the closest surface rupture to the epicenter is located around 5 km to the east, along the Narli segment of the Dead Sea (transform)

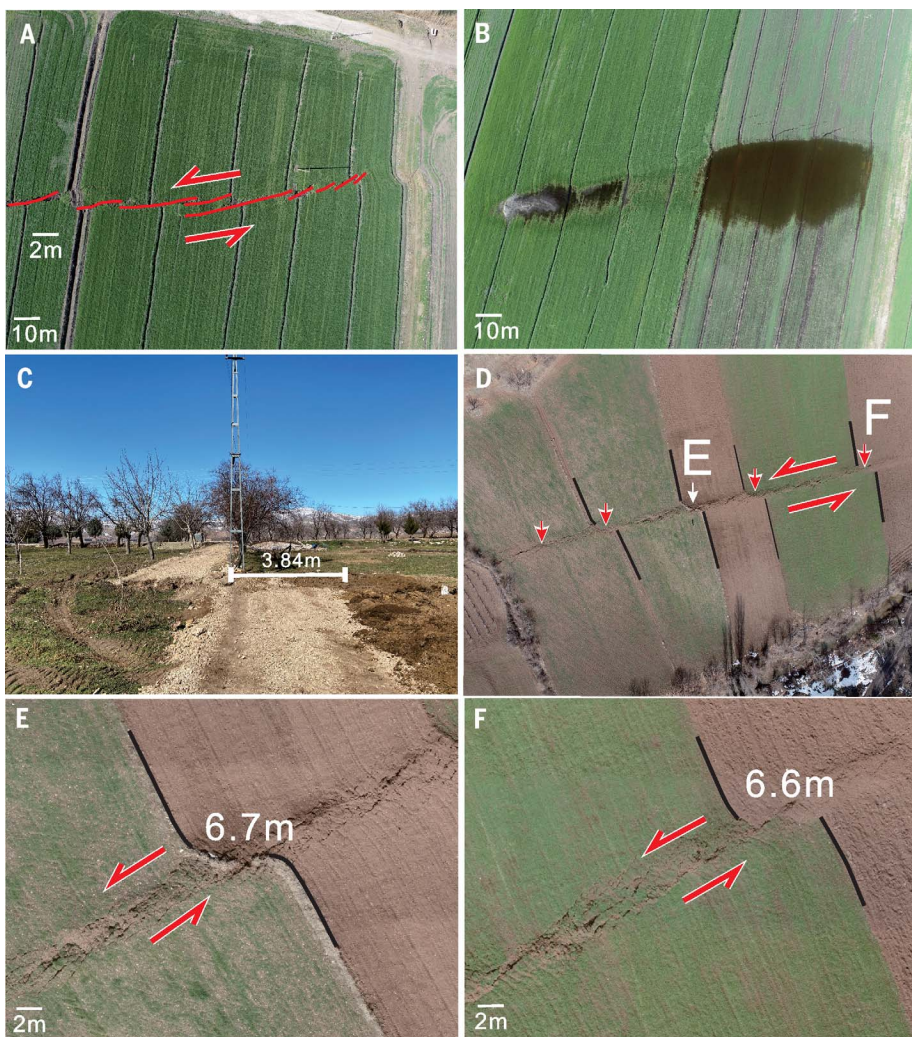


Fig. 5. Surface expression of maximum displacement area on the EAFZ, located at the triple junction where the Dead Sea transform intersects the East Anatolian transform. (A) A farm field is offset by synthetic en echelon pattern faults. (B) A newly formed sag basin (indicated by recent pond) formed through subsidence along an extensional jog in the fault system. (C) A road is offset by 3.84 m. All observations indicate sinistral motion. (D) The fault cuts through the field and exhibits the largest ground offset that we observed. (E and F) Close-up views showing that the displacement is accommodated across a 3- to 4-m-wide zone of distributed deformation, or damage zone (6*l*). Locations of images (E) and (F) are labeled in (D).

fault zone, extending around 7.2 km from north to south (Fig. 3). The geometry of this fault strand is generally north-south striking (ranging between 346° and 030°), on nearly vertically dipping (78° to 89°) planes, and the surface lateral offsets are around 2 to 2.5 m. (Figs. 3 and 4) [(*II*), data S1 and S2], with some unusual oblique reverse-slip motions at the tips of the rupture areas and along isolated pop-up pressure ridge structures, as described along other strike-slip fault systems (27, 28).

The Narlı fault strand of the Dead Sea transform fault merges with the main EAFZ about 47.5 km northeast of the epicentral region that marks the triple junction between the Arabian, African, and Anatolian plates (Figs. 1 and 3).

The rupture propagated from the Narlı segment to the EAFZ during the initial 10 to 25 s of the M_w 7.8 event (Fig. 2), depending on which data are used for the seismic inversion (8, 29). The EAFZ generally has larger horizontal offsets than those of the Narlı fault segment (Fig. 2, C to F), where the first M_w 7.8 earthquake initiated, and the energy release spectra (Fig. 2A) were noticeably less on the Narlı segment. The strike of the EAFZ in our field observations ranges from 347° to 110° along 300 km, and the horizontal ground offsets vary from 3.4 to 6.7 m (Figs. 3 and 5, D, E, and F) [(*II*), imagery S2 to S5 and data S2].

The area of maximum offset from this earthquake event is located 47.5 km to the

northeast of the epicenter (37.5830042°N, 37.316717°E), along the Pazarcık segment of the EAFZ at the triple junction between the three plates (Fig. 3). The maximum displacement is in a farm field in which individual previously linear roads and crop rows are offset by the 051° striking fault from 6.5 to 6.7 m along a 200-m-long strand of the fault. The images we documented show the undisturbed offsets soon after the earthquakes, but because they are in farm soils, they were subsequently obscured by plowing of the soil for planting the next harvest of crops. Neither clear fault planes nor clear vertical offsets were observable at this location (Fig. 5D) [(*II*), data S2], with the displacement accommodated across a 3- to 4-m-wide deformation zone (Fig. 5, E and F) [(*II*), data S2].

Our observations indicate that the greatest ground deformation and area of maximum slip is not located in the epicenter region. Instead, as the fault rupture propagated over 90 s, it took 24 s for the main rupture with the highest energy release (Fig. 2A) to occur on the Pazarcık segment of the EAFZ (Fig. 2, C to F). The rupture can be interpreted to have propagated at 2.03 km/s from where it initiated on the Narlı fault to the location where greatest energy was released at the intersection of the Narlı and East Anatolian faults, also yielding the largest displacements. The maximum displacement and energy release occurred almost precisely when the rupture propagated to the main EAFZ. Our observations of the distance that the rupture traveled to the maximum offset area when the maximum energy was released are slightly lower than that from geophysical numerical rupture models that use joint kinematic inversion of high-rate global navigation satellite system (HR-GNSS) and strong motion data, which suggest supershear rupture propagation velocities of up to 3.2 km/s for the M_w 7.8 event (8), but are consistent with a slow moment release on the Narlı fault during the first 12 s (29). Twenty min after this event, new earthquakes started propagating northeast and southwest along the EAFZ [(*II*), imagery S1].

Seven hours and 40 min after the main M_w 7.8 event, a M_w 4.5 aftershock struck the junction of the east-west Ç-SF with the EAFZ on the Sürgü fault (Fig. 1) (10) and activated seismicity on the entire Ç-SF system [(*II*), imagery S6]. One hour 20 min after the M_w 4.5 earthquake, the M_w 7.5 Elbistan event occurred in the center of the Ç-SF, possibly induced by stress changes caused by the earlier earthquakes (2). During our observations of the Ç-SF, the mountains were covered with thick snow, followed by springtime torrential rains and disastrous flooding, partially erasing many of the delicate fault surface features and hampering further observations of ground offsets and fault planes. Thus, no convincing offset was measurable on the Ç-SF during our fieldwork, although the rupture

surfaces and slip lineations were visible and measured (fig. S5, A to F). However, reports exist indicating that the C-SF has around 7 to 8 m of local horizontal offsets, but these have not been confirmed with quantified field observations (30, 35).

Vertical offsets on the faults, ranging from 0.5 to 1.7 m on different fault segments, are not as large as the major horizontal displacements. Vertical offsets occur either as ground ruptures or as oblique thrust-strike slip offsets on pressure ridges along strike-slip faults (figs. S5, A, B, and E) or as oblique-normal displacements along extensional jogs and sag basins (Fig. 5B), which is consistent with the remote sensing observations derived from ESA Sentinel-1 radar image pairs acquired on 28 January 2023 and 10 February 2023 (29, 30).

Other surface deformation features

En echelon fracture patterns are the most common surface deformation style along the fault zone (Figs. 4 and 5A) [(11), data S1 and S2]. The surface deformation, especially in clays and unconsolidated alluvium, is characterized in many places by a series of discontinuous synthetic en echelon faults that theoretically should lie at an acute angle to the main fault at depth, and the en echelon faults on the surface may merge with a major fault plane near or above the brittle-ductile transition (5–7, 36–39). This pattern is consistent with the nearly parallel but slightly oblique relationships between the measured surface faults and the recorded seismic moments, indicating sinistral motions (fig. S4, A to I). Ground deformation in this pattern gradually decreases at the end of the individual deformation belts and is picked up by the next synthetic en echelon fault.

The surface ruptures and newly formed faults do not always follow topographic changes or preexisting weak surfaces. Some of the ruptures cut through the centers of basins, and others cut across the topographic highs directly, instead of following known fault traces, which is inconsistent with expectations that the new ruptures follow known active faults or topographic changes. Old fault-related sag basins and pressure ridges were activated by these events, and there are also some newly formed sag and small pull-apart basins and pressure ridges (39) that emerged along the faults, often bordered by splays (Figs. 4, E and F, and 5B).

Progressive development of through-going fault surfaces with increasing displacement in unconsolidated soils

The mechanisms by which strike-slip fractures propagate and coalesce into major through-going faults in rocks and other materials have been examined experimentally, theoretically, and with a limited number of field observations (36, 40–43). Many of the field examples show that large strike-slip faults often form by

the linking of many en echelon faults or fractures [for example, (9, 39, 43, 44–49)], a hypothesis that our observations confirm. Previous studies have generally suggested that the propagation and growth of fractures into faults is variable and depends on the material properties of the affected area, the stress and strain conditions, and the presence or absence of pre-existing fractures. However, relatively few studies have examined fault propagation in soils or

unconsolidated sediments, with some exceptions noted above (1–4, 49–52) and some theoretical studies [for example, (50, 53)]. The detailed imagery and maps presented here [(11), data S1 to S3] offer an unprecedented view of the propagation and development of surface fault features in soils and bedrock associated with two major earthquakes.

Snapshots of our drone images and maps of the EAFZ ruptures in farm field soils [(11), data

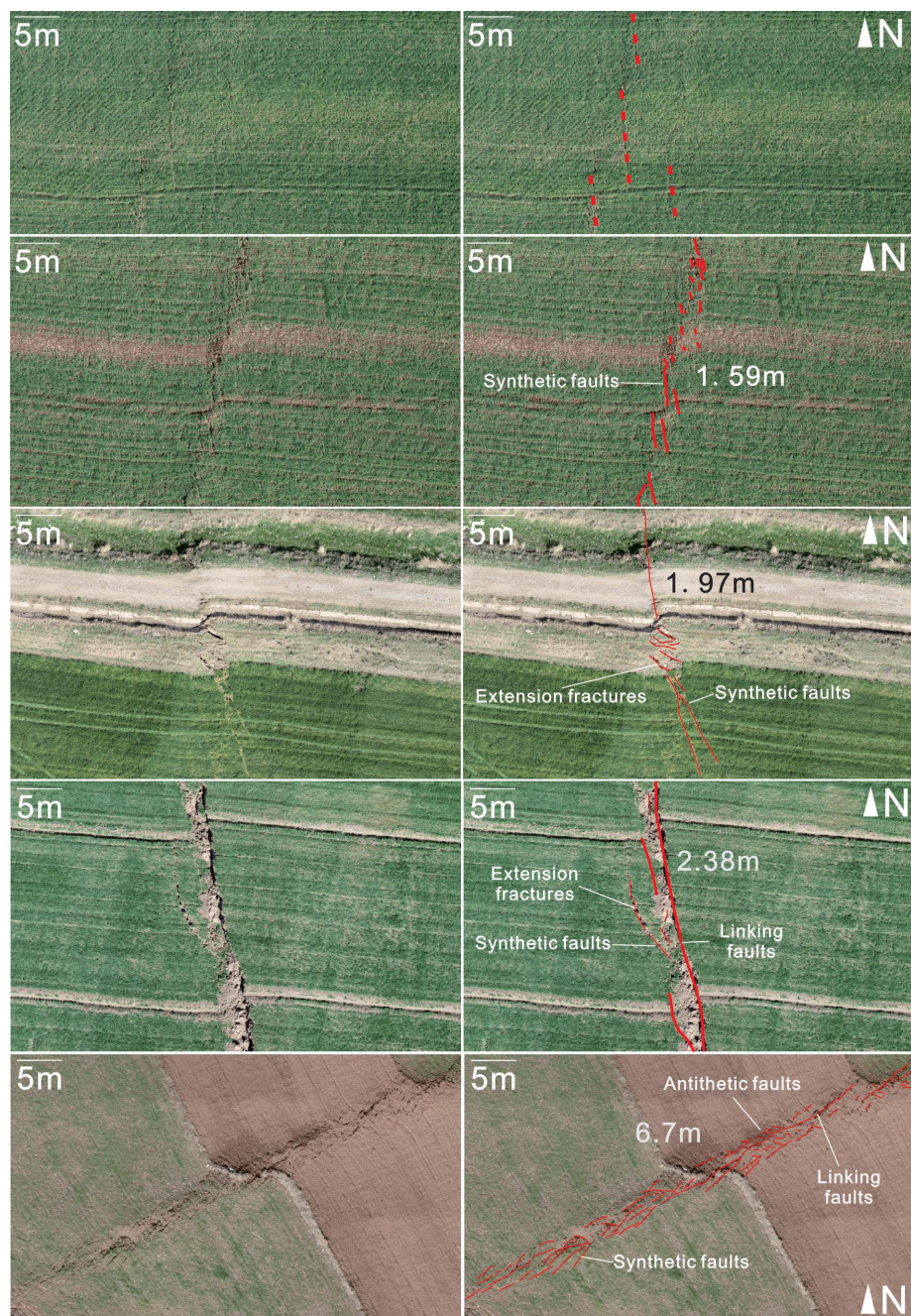


Fig. 6. Progressive development of through-going fault planes from initial series of en echelon faults along the EAFZ. (Left) Uninterpreted images. (Right) The same images including our interpretations of the new fault planes, with increasing displacements from top to bottom. Locations of images are given in (11), data S1.

S1] are shown in Fig. 6 in a progression from low displacements at top to the 6.7-m maximum displacements at bottom [(II), data S2]. There is a progression from small, isolated, nearly parallel fractures at the smallest displacements to synthetic en echelon faults at about 1.5-m displacements, with through-going linking faults parallel to the main fault beginning to cut both synthetic and antithetic en echelon faults at displacements greater than 2.3 m. The largest offset areas are characterized by through-going faults and continued development of en echelon faults, defining a wider damage zone for the main fault. The progressive structural development of the fault features in soils is very similar to that in rocks with different material properties (48–53). This observation suggests that the material properties may be less important than other factors (stress and strain) in determining the structural development of large-scale, high-displacement faults in unconsolidated sediments.

Discussion and implications

Our mapping of the surface deformation features of the earthquakes of 6 February 2023 provides new information on the distribution of slip along two major continental transform faults and provides insight into rupture propagation and slip transfer on complex fault systems. Our rapid deployment to the field made it possible to obtain high-quality uncrewed aerial vehicle (drone) and ground observations of ephemeral surface deformation features. These data, together with the corresponding seismic data, illustrate the process through which tectonic plates interact within two large-scale continental transform systems. The dual M_w 7.8 and M_w 7.5 earthquakes demonstrate how the sudden motion of one plate (Arabia, moving to the north) can lead to the response to that motion by another plate (Anatolia, moving to the west). Thus, the observed surface displacements correlated with the seismic moment release provide insight into how continental plate tectonic processes occur with the coupled rupturing of two plate boundaries, and how the surface expression of these plate movements is formed in the geological and geomorphic record.

Our observations of surface displacements (Fig. 2, C to F) add to the existing knowledge base of the patterns of surface rupture for major earthquakes. For example, a broadly similar pattern of surface displacement was documented from the 2002 Denali (Alaska) earthquake, with branching of fault strands on the Denali and Totschunda faults and maximum fault displacement far from the epicenter (3). However, in general maximum surface offsets far from the epicenter, as we have documented, are not common (4). We found that the largest ground offset is not near the epicenter within the Narli segment of the Dead Sea transform

fault. Rather, the largest offset is 47.5 km to the northeast at the intersection of the Dead Sea and East Anatolian fault systems. This situation is unusual because observations from other earthquake events typically show that fault junctions foster rupture arrest, not increases in slip (54–56). We suggest that the observed spike in the relative seismic moment rate (energy release in newton-meters per second), which occurred 24 s after the origin time, relates to the time when the Narli rupture intersected with the EAFZ, which then “exploded” with 6.7 m of slip at the intersection (at the triple junction plate boundary). The rupture then became bilateral, activating the entire central and southern EAFZ transform plate boundary. This burst of released energy, with maximum fault slip, may be due to this portion of the EAFZ having accumulated several hundred years of stress build-up (25–28). On the basis of seismic waveform modeling, the rupture propagation on the EAFZ was at supershear velocities ($>\sim 3$ km/s), which is perhaps 1.55 times the shear wave velocity, creating a “Mach cone” that is analogous to a sonic boom in the air (8, 57). However, our observations suggest that the initial rupture propagation on the Dead Sea transform (Narli fault) was at a subshear velocity and accelerated only after transfer to the EAFZ, where the rupture became bilateral (29, 57). Our data show that the maximum slip on the EAFZ (6.7 m) was very near the intersection of the two fault systems, about 5 to 10 km southwest of the maximum slip location predicted by the US Geological Survey finite fault model [(32), doc. S3] (29).

Our data, together with the analysis of the seismic data and stress modeling reported elsewhere, relate to the important question of how the slip migrated from the EAFZ to the Ç-SF. More than 7 hours after the rupture propagated north along the EAFZ, a M_w 4.5 earthquake occurred at the junction with the easternmost portion of the Ç-SF. The east-west Çardak-Sürgü system then became seismically active, followed some 86 min later by the M_w 7.5 earthquake [(II), imagery S1]. The timing suggests that the M_w 7.5 event on the Ç-SF may have been triggered by a stress change or other fault parameters, such as a pore pressure increase, that were altered because of the M_w 7.8 event. The M_w 7.5 earthquake produced an abundant aftershock sequence on the Ç-SF. However, the aftershocks show that slip did not reconnect with the EAFZ but unexpectedly turned northeast along a new fault rupture plane on the Ciglik fault (10), which is parallel to the EAFZ (Figs. 1B and 3).

The large distance (47.5 km) between the epicenter location and the area of maximum fault displacement calls into question the interpretation of historical earthquake catalogs that probably record the location of the most damaged population center rather than the epicenter where historical earthquakes were initiated.

These earthquake catalog locations can be interpreted as the locations of maximum energy release.

Our data address the question of where the largest surface deformation may be expected for a large earthquake. Our field investigation shows that surface fault deformation is typically distributed on a series of en echelon faults within a several-meter-wide damage zone, whereas at depth, the maximum displacement may be on a discrete fault plane where the individual en echelon faults merge (1–3). The shape of the displacement field may be complex and intersect the surface obliquely from the hypocentral location for a dipping fault.

The M_w 7.8 and M_w 7.5 earthquakes of February 2023 provide a wealth of information on fault rupture propagation, how slip is transferred between fault systems, how this behavior is related to large-scale linked tectonic plate motions, and how seismic and other geophysical data correlate with observable ground deformation features. Our ground-truth observations provide quantitative measurements of surface offsets and associated deformation. Continued comparison of ground deformation, dynamic rupture models, Coulomb stress models, finite fault models, and other geophysical measurements may improve understanding of the physics of large earthquakes and how individual fault systems accommodate global plate motions, and this knowledge may contribute to protecting society from the consequences of major earthquakes.

REFERENCES AND NOTES

1. G. P. Biasi, R. J. Weldon, *Bull. Seismol. Soc. Am.* **96**, 1612–1623 (2006).
2. G. P. Biasi, S. G. Wesnousky, *Bull. Seismol. Soc. Am.* **106**, 1110–1124 (2016).
3. P. J. Haeussler et al., *Earthq. Spectra* **20**, 565–578 (2004).
4. M. A. Hemphill-Haley, R. J. Weldon, *Bull. Seismol. Soc. Am.* **89**, 1264–1279 (1999).
5. US Geological Survey, Earthquake Lists, Maps, and Statistic (accessed March 18, 2023); <https://www.usgs.gov/natural-hazards/earthquake-hazards/lists-maps-and-statistics>.
6. R. Schmitt, M. Herman, W. Barnhart, K. Furlong, H. Benz, The 2023 Kahramanmaraş, Turkey, Earthquake Sequence, (USGS Geologic Hazards Center, March 28 2023); <https://storymaps.arcgis.com/stories/355bcf8b3c5941e683d4f258e8fb2dfa>.
7. T. M. Kusky, E. Bozkurt, J. Meng, L. Wang, *J. Earth Sci.* **34**, 291–296 (2023).
8. D. Melgar et al., *Seismica* **2**, 3 (2023).
9. P. M. Mai et al., *The Seismic Record* **3**, 105–115 (2023).
10. Ö. Emre et al., *Bull. Earthquake Eng.* **16**, 3229–3275 (2018).
11. J. Meng et al., Other supplementary materials for Surface deformations of the February 6, 2023 earthquake sequence, eastern Türkiye. figshare (2023); <https://doi.org/10.6084/m9.figshare.24872043>.
12. D. Whiteman et al., *Geology* **51**, 673–677 (2023).
13. A. C. Şengör, C. Zabcı, B. A. Natal'in, *Continental Transform Faults in Encyclopedia of Geology* (Elsevier, 2021), pp. 913–929.
14. A. C. Şengör, N. Canitez, *Geodyn. Ser. 7*, 205–216 (1982).
15. J. Dewey, A. C. L. Şengör, *Geol. Soc. Am. Bull.* **90**, 84–92 (1979).
16. D. McKenzie, *Earth Planet. Sci. Lett.* **29**, 189–193 (1976).
17. E. Bozkurt, *Geodin. Acta* **14**, 3–30 (2001).
18. X. Le Pichon, C. Kremer, *Annu. Rev. Earth Planet. Sci.* **38**, 323–351 (2010).
19. A. Şengör et al., *Annu. Rev. Earth Planet. Sci.* **33**, 37–112 (2005).
20. F. A. Capitanio, *Earth Planet. Sci. Lett.* **448**, 122–132 (2016).
21. C. Faccenna et al., *Rev. Geophys.* **52**, 283–332 (2014).
22. L. Jolivet et al., *Tectonophysics* **597–598**, 1–33 (2013).

23. A. Şengör, M. Yazıcı, *Mediterranean Geoscience Reviews* **2**, 327–339 (2020).
24. J. Meng et al., *Sci. Rep.* **11**, 6486 (2021).
25. N. N. Ambraseys, *Geophys. J. Int.* **96**, 311–331 (1989).
26. B. Aktug et al., *J. Geodyn.* **94–95**, 1–12 (2016).
27. R. Reilinger et al., *J. Geophys. Res. Solid Earth* **111**, B5 (2006).
28. A. Hubert-Ferrari et al., *Earth Planet. Sci. Lett.* **538**, 116152 (2020).
29. D. E. Goldberg et al., *The Seismic Record* **3**, 156–167 (2023).
30. N. G. Reitman et al., (2023). Fault rupture mapping of the 6 February 2023 Kahramanmaraş, Türkiye, earthquake sequence from satellite data. US Geological Survey Data Release (2023); <https://doi.org/10.5066/P98517U2>.
31. S. Barbot et al., *Seismica* **2**, 2 (2023).
32. Materials and methods are available as supplementary materials.
33. D. Peringel, I. Çemen, *Tectonophysics* **172**, 331–340 (1990).
34. Y.-S. Kim, J. R. Andrews, D. J. Sanderson, *Geosci. J.* **4**, 53–72 (2000).
35. L. Dal Zilio, J.-P. Ampuero, *Commun. Earth Environ.* **4**, 71 (2023).
36. L. N. Y. Wong, Y. Zhang, *J. Geophys. Res. Solid Earth* **124**, 10916–10939 (2019).
37. A. Sylvester, *Geol. Soc. Am. Bull.* **100**, 1666–1703 (1988).
38. Y. Cheng, L. N. Y. Wong, C. Zou, *Eng. Geol.* **195**, 312–326 (2015).
39. P. Mann, M. R. Hempton, D. C. Bradley, K. Burke, *J. Geol.* **91**, 529–554 (1983).
40. M. Doblas, *Tectonophysics* **295**, 187–197 (1998).
41. A. G. McGrath, I. Davison, *J. Struct. Geol.* **17**, 1011–1024 (1995).
42. P. A. Cowie, Z. K. Shipton, *J. Struct. Geol.* **20**, 983–997 (1998).
43. Y.-S. Kim, D. C. P. Peacock, D. J. Sanderson, *J. Struct. Geol.* **25**, 793–812 (2003).
44. D. A. Rodgers, in *Sedimentation in Oblique-Slip Mobile Zones*, P. F. Ballance, H. G. Reading, Eds. (Wiley, 1980), pp. 27–41.
45. T. Kusky, W. Kidd, D. Bradley, *J. Geodyn.* **7**, 105–133 (1987).
46. T. Kusky, C. Robinson, F. El-Baz, *J. Geol. Soc. London* **162**, 871–888 (2005).
47. B. Tikoff, C. Teyssier, *Geology* **20**, 927–930 (1992).
48. D. Faulkner, A. Lewis, E. Rutter, *Tectonophysics* **367**, 235–251 (2003).
49. E. J. Willemse, D. C. Peacock, A. Aydin, *J. Struct. Geol.* **19**, 1461–1477 (1997).
50. D. Loukidis, G. D. Bouckovalas, A. G. Papadimitriou, *Soil. Dyn. Earthquake Eng.* **29**, 1389–1404 (2009).
51. T. M. Kusky et al., *J. Earth Sci.* **21**, 910–922 (2010).
52. B. A. Brooks et al., *Sci. Adv.* **3**, e1700525 (2017).
53. J. Shi, L. Guan, D. Zhuang, X. Chen, D. Ling, *J. Rock Mech. Geotech. Eng.* **15**, 2973–2993 (2023).
54. Y. Cheng, Y. Ben-Zion, *Geophys. Res. Lett.* **47**, e2020GL089650 (2020).
55. R. D. Koehler et al., *Seismol. Res. Lett.* **92** (2A), 823–839 (2021).
56. J. Liu-Zeng et al., *Earthquake Research Advances* **2**, 100140 (2022).
57. B. Delouis, M. van den Ende, J. P. Ampuero, *Bull. Seismol. Soc. Am.* **113**, 1–15 (2023).
58. Advanced Spaceborne Thermal Emission and Reflection Radiometer, (ASTER) Global Digital Elevation Model, version 3 (Jet Propulsion Laboratory, 2019); <https://asterweb.jpl.nasa.gov/gdem.asp>.
59. V. Karabacak et al., *J. Geol. Soc. London* **180**, jgs2023-jgs2023-020 (2023).
60. D. Delvaux, B. Sperner, in *New Insights into Structural Interpretation and Modelling*, D. A. Nieuwland, Ed., Geographical Society Special Publications vol. 212 (Geographical Society of London, 2003), pp. 75–100.
61. E. Hussain, S. Kalaycioglu, C. W. D. Milliner, Z. Çakir, *Nat. Rev. Earth Environ.* **4**, 287–289 (2023).

ACKNOWLEDGMENTS

We are grateful to the people of Türkiye for their assistance during the field work. We thank D. E. Goldberg, J. Nevitt, B. Sherrod, E. Van Dyke, L. Hanson, C. Barrera-Lopez, R. Chidlow, J. Hardebeck,

S. Hecker, and three anonymous readers for their review comments. Any use of trade, firm, or product names is for descriptive purposes only and does not imply endorsement by the China University of Geosciences, Middle East Technical University, Hakkari University, or the US government. **Funding:** This work was supported by the National Natural Science Foundation of China, 41888101 (T.K. and L.W.) and 91755213 (T.K., L.W., and E.B.); the State Key Lab of Geological Processes and Mineral Resources, China University of Geosciences (Wuhan), MSFGPMR2022-7 (L.W.); and the US Geological Survey Earthquake Hazards Program (W.D.M.). **Author contributions:** Conceptualization: T.K. and W.D.M. Methodology: J.M. and T.K. Investigation: J.M., T.K., W.D.M., E.B., M.N.B., and L.W. Visualization: J.M., W.D.M., and T.K. Funding acquisition: T.K., L.W., and E.B. Project administration: T.K. and L.W. Supervision: T.K., W.D.M., and E.B. Writing – original draft: J.M., T.K., and W.D.M. Writing – review and editing: J.M., T.K., W.D.M., E.B., and L.W. **Competing interests:** The authors declare no competing interests. **Data and materials availability:** All data are available in the main text, the supplementary materials, and at the locations listed at (11), the latter directing to imagery S1 to S7 and data S1 to S3. **License information:** Copyright © 2024 the authors, some rights reserved; exclusive licensee American Association for the Advancement of Science. No claim to original US government works. <https://www.science.org/about/science-licenses-journal-article-reuse>

SUPPLEMENTARY MATERIALS

science.org/doi/10.1126/science.adj3770

Materials and Methods

Supplementary Text

Figs. S1 to S7

Tables S1 to S3

References (62–69)

Submitted 23 June 2023; resubmitted 18 September 2023

Accepted 8 December 2023

10.1126/science.adj3770